ISSN (Print) 1226-1750
ISSN (Online) 2233-6656
Journal of Magnetics 22(2), 203-213 (2017) https://doi.org/10.4283/JMAG.2017.22.2.203

Design and Analysis of Lorentz Force-type Magnetic Bearing Based on High Precision and Low Power Consumption

Guofeng Xu, Yuanwen Cai, Yuan Ren*, Chaojun Xin, Yahong Fan, and Dengliang Hu

Equipment Academy, 101416, Beijing, China

(Received 11 October 2016, Received in final form 9 May 2017, Accepted 11 May 2017)

Magnetically suspended control & sensitive gyroscope (MSCSG) is a novel type of gyroscope with the integration of attitude control and attitude angular measurement. To improve the precision and reduce the power consumption of Lorentz Force-type Magnetic Bearing (LFMB), the air gap flux density distribution of LFMB has been studied. The uniformity of air gap flux density is defined to qualify the uniform degree of the air gap flux density distribution. Considering the consumption, the average value of flux density is defined as well. Some optimal designs and analyses of LFMB are carried out by finite element simulation. The strength of the permanent magnet is taken into consideration during the machining process. To verify the design and simulation, a high-precision instrument is employed to measure the 3-dimensional magnetic flux density of LFMB. After measurement and calculation, the uniform degree of magnetic flux density distribution reaches 0.978 and the average value of the flux density is 0.482T. Experimental results show that the optimal design is effective and some useful advice can be obtained for further research.

Keywords : Magnetically suspended control & sensitive gyroscope (MSCSG), Lorentz Force-type Magnetic Bearing (LFMB), electromagnetic torque, uniformity

1. Introduction

Due to a variety of priority of zero friction, high-speed operation, active vibration suppression, long life span and great potential of high control accuracy [1-4], active magnetic bearings (AMBs) have been successfully employed for many space missions as ideal actuator for the attitude control of the spacecraft [5-8] with high accuracy output torque and small vibration disturbance. The maglev flywheel with shaft tilting can not only output 1 degree-of-freedom (DOF) attitude control torque by changing the value of angular momentum just like the traditional ones, but also can change the direction of angular momentum to output 3 DOF attitude control torque. This kind of maglev flywheel can rapidly inhibit the instantaneous large disturbance torque to meet the attitude control needs of high-precision and high-stability, which is an ideal actuator to achieve high-resolution reconnaissance missions [9]. In recent years, researchers have begun to develop inertial sensors based on AMBs, named magnetically suspended sensitive gyroscope (MSSG) [10, 11], which is used to measure attitude angle or angular velocities. To realize the hyperstable and hyperquiet attitude control of space-based platform, a new concept gyroscope named magnetically suspended control & sensitive gyroscope (MSCSG) is put forward, which integrates attitude control function and attitude angular rate measurement function. Its rotor with high speed is driven by Lorentz Force-type Magnetic Bearing (LFMB) to tilt in all directions and control the attitude with precise torque. And the attitude angular velocities can be calculated by the control currents of LFMB.

The electromagnetic force generated by LFMB is determined by the ampere force law($F=BIL$) and the tilting torque is the product of the electromagnetic force and arm. According to the rotor dynamics equation and the ampere force law, the current of the coil can be directly calculated and input into LFMB to drive the rotor tilt to the desired tilting angle. So it is clear that precision of tilting torque is mainly deterimined by the magnetic flux density of LFMB, as well as the precison of measurement. Related researches about the magnetic flux density distribution of the Lorentz force-type devices can be summarized as follows:

©The Korean Magnetics Society. All rights reserved.
*Corresponding author: Tel: +86-010-6636-4384
Fax: +86-010-6636-4194, e-mail: renyuan823@aliyun.com

© 2017 Journal of Magnetics

(1) A Lorentz force-type integrated motor-bearing is studied and the magnetic flux density generated by the rotor permanent magnets is assumed as a sinusoidal waveform verificated by measurement and the mortoring torque is modeled, and the rotor is controled to tilt with stability and robutness [12]. Stephens *et al.* designed a new type of self-bearing motor, which used the Lorentz-type forces to produce both bearing force and motoring torque, and the tradeoff between motoring torque and bearing force is eliminated. Taken the distributing non-uniformity into account, the air gap flux density has been approximated to be a sine cure. And the error between the sinusoidal approximation and the measured distribution is more than 20 %, due to it contains odd orders of harmonic [13].

(2) The magnetic flux density of a Lorentz force-type axial actuator is deterimined by the product of the coercive force, the length of permanent magnet and the permeances of magnetic flux. And the permeances of magnetic flux are defined as complex nonlinear integral equations [14]. Nobuyuki Kurita and Yu Y.J analyzed the flux density distribution in the air gap of a magnetically suspended flywheel by the finite element method in detail, and the nonlinear magnetic torque has been modeled. However, quantitative research has not been conducted [15, 16].

(3) J Abrahamsson analyzed a compact conical Lorentz force self-bearing motor. The machine possesses the ability of magnetic positioning in axial as well as radial directions that can be achieved by skewing the windings of a radial flux machine. The distributing nonuniformity of the flux density in the air gap has been considered, and it is assumed that the magnetic field can be approximated by a square wave [17].

(4) Xu X.B. *et al.* proposed a novel suspension method which consists with the conical MB and Lorentz MB. Based on the assumption that the magnetic flux density in the gap is homogenous, both the magnetic force and its moment are linear with the control current of the Lorentz MB. In addition, the Lorentz MB can realize the continual tilting according to the different input signal [18].

It is clear that the non-uniform distribution of magnetic flux density has not get changed by all the researchs above. This paper is aimed to design a new LFMB with uniform magnetic flux density distribution. At the same time, taking into account the power consumption, the magnetic intensity of LFMB should be improved by some additional optimal designs.

The remainder of this paper is organized as follows: In Section 2, the MSCSG is described and its characteristics are analyzed in detail. Next, the precise mathematical model of electromagnetic torque for basic LFMB is established to analyze the key factors that affect the accuracy of the torque and its flux density is discussed preliminarily in Section 3. In Section 4, some optimal designs and analyses of LFMB are carried out to improve the uniform degree of the air gap flux density distribution and the average value of flux density. The magnetic flux density of LFMB is measured in Section 5. Follow on, Section 6 concludes this paper.

2. Description of MSCSG and its Characteristics

2.1. Description of MSCSG system

The MSCSG studied in this paper consists of rotor, stator and a stator house which the stator is fixed to. Its schematic diagram is drawn in a cross-sectional situation of two dimensions in Fig. 1. The rotor is designed into a flat structure to get larger ratio of moments of inertia and

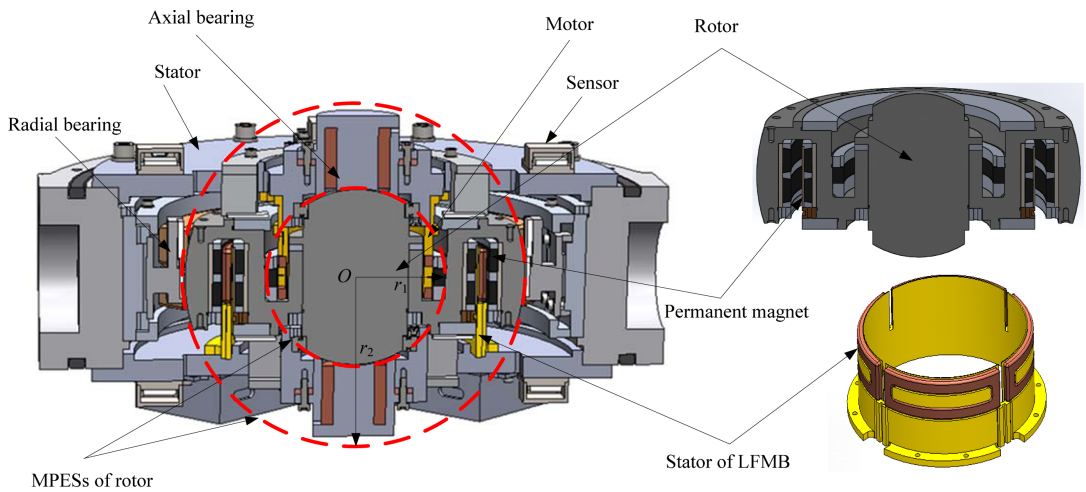

Fig. 1. (Color online) Configuration of MSCSG.

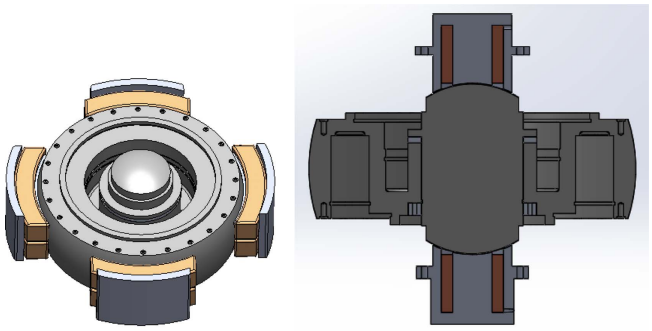

(a) Radial spherical bearing (b) Axial spherical bearing

Fig. 2. (Color online) Configuration of radial spherical bearing and axial bearing.

mass, which will reduce the quality of the rotor as well as the volume and power consumption of the axial/radial bearing. Both the magnetic pole envelope surfaces (MPESs) of the stator and the rotor are spherical surfaces. The rotor of the MSSG is a type of incomplete spherical with different radiuses of MPESs in axial and radial, which is made of magnetic material in whole. Radial and axial radiuses of the rotor are r_1 and r_2 respectively. And the stator of LFMB is installed at the middle of the central cavity of rotor. When the MPESs of the MSCSG are ideal spherical surfaces, the magnetic forces over the entire surface of the rotor will pass through its geometric center and no disturbing torques are generated, that is, no drift errors generated.

The radial spherical magnetic bearing is employed to control the translation in x, y direction and differentially driven by two pairs of magnetic poles, as shown in Fig. 2(a). Its x channel is separated from y channel by isolation ring, so the magnetic circuit of x and y channel is decoupled. Besides, the radial translation of 2 DOF and the radial rotation of 2 DOF are also decoupled when the mass center of the radial magnetic bearing spherical magnetic pole and the gyro rotor are coincident. The axial spherical magnetic bearing is employed to control the translation in z direction and differentially driven by one pair of magnetic poles, as shown in Fig. 2(b). These 2 bearings are all pure electromagnetic bearings with adjustable stiffness, controllable precision and lowest coupling. As shown in Fig. 1, its radial rotation of 2 DOF is realized by LFMB. It is obvious that the translation of 3 DOF and the radial rotation of 2 DOF are decoupled from structures and their controllers can be designed separately.

2.2. Tilting torque with high-precision and high bandwidth

With MSCSG rotor supported elastically, the high-speed rotor of MSCSG can tilt in all direction at the limited gap and the bandwidth of control torque for MSCSG can be enhanced largely. Compared with the frame torque, the tilting torque has higher precision and bandwidth. The reasons are mainly reflected as follows:

(1) The mode of driving force: the frame torque is rotary driven indirectly, which will bring friction and transmission delay. While, the tilting torque is directly liner-driven and there is no friction and transmission delay.

(2) The direction of driving force: the frame torque is driven by tangential component of magnetic force, which is nonlinear with the rotation angle position and makes the control precision low. The tilting torque is driven by normal force, which is liner with displacement and has high control precision.

(3) Detection accuracy of motion: the frame torque is measured by angle with minimum range and the precision is low. While, the tilting torque is measured by displacement with maximum range and the precision is high.

Through the rotation of frame or the changing speed, MSCSG can output low bandwidth attitude control torque as an inertial actuator. Besides, the rotor is driven by small current to tilt at all direction, so the bandwidth and precision of control torque can be largely enhanced, which can be just employed to suppress the periodical vibration of space-based platform. And, it is a new way to solve high-frequency angular vibration problem of excessively steady and static platform.

3. Design and Analysis of Basic LFMB

3.1. Modeling and analysis of precise electromagnetic torque for basic LFMB

The structure of basic LFMB can be seen in Fig. 3. The inside and outside PM rings are arranged in the circumferential of the rotor groove. In order to make the magnetic circuit close, the inside and outside PMs are opposite, and a stable magnetic field is generated between them. 4 coils with same turns are located on the stator frame which is at the gap between the inside and outside PMs. And these 4 coils are used in series with pairs. The sensors are employed to detect the axial displacement of rotor when it is tilting and the tilting angle can be calculated.

As is shown in Fig. 3, the origin of the coordinate system is located at the geometric center of the LFMB's stator. The x-axis and y-axis are defined as coinciding with the center line of the two pairs of coils, and z-axis is within the right-hand rule. The tilting angles around the x-axis and y-axis are defined as α and β respectively. 4 coils have the same circumferential angle (2φ). Coil i can be expressed as

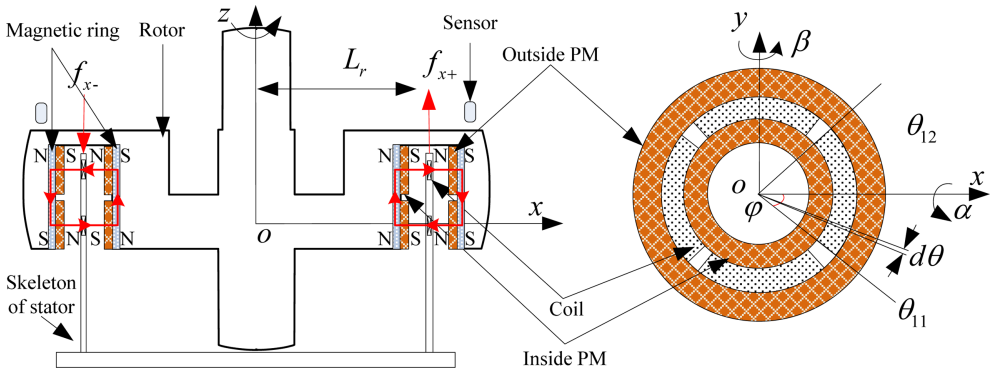

Fig. 3. (Color online) Structural schematic diagram of LFMB.

$$\text{Coil}_i = \left(\frac{(i-1)\pi}{2} - \varphi, \frac{(i-1)\pi}{2} + \varphi\right) \quad i = 1, 2, 3, 4 \qquad (1)$$

The electromagnetic force is generated by LFMB according to ampere force law. As is shown in Fig. 3, the torque generated by the infinitesimal $L_r d\theta$ of one turn of the upper part of one coil can be described as

$$d\boldsymbol{T}_i = \boldsymbol{r} \times df_i = \begin{bmatrix} L_r \sin\theta \\ -L_r \cos\theta \end{bmatrix} BI_i L_r d\theta \qquad (2)$$

Where, I_i is the current of coil i, L_r is the radius of stator of LFMB, B is the flux density and assumed to be a constant.

Actually, the coil is a regular shape made of evenly arranged copper wires. In detail, the number of layers is N and the number of copper wires in each layer is M. The thickness of one coil is d. The accurate $d\boldsymbol{T}_i$ is

$$d\boldsymbol{T}_i = BI_iN\left(\left(L_r - \frac{d}{2} + \frac{d}{2M}\right)^2 + \left(L_r - \frac{d}{2} + \frac{3d}{2M}\right)^2 + \cdots + \left(L_r + \frac{d}{2} - \frac{d}{2M}\right)^2\right)\begin{bmatrix} \sin\theta \\ -\cos\theta \end{bmatrix} d\theta \qquad (3)$$

Then, the total torque $\boldsymbol{T}$ of the upper and lower parts of 4 coils is

$$\boldsymbol{T} = \sum_{i=1}^{4} \boldsymbol{T}_i = 4NB \sum_{k=1}^{M} \left(Lr - \frac{d}{2} + \frac{2k-1}{2M} d\right)^2 \sin\varphi \begin{bmatrix} I_2 - I_4 \\ I_3 - I_1 \end{bmatrix} \qquad (4)$$

Where, I_2 and I_4, I_1 and I_3 are equal in magnitude and opposite. Then $\boldsymbol{T}$ can be described as

$$\boldsymbol{T} = 8NB \sum_{k=1}^{M} \left(Lr - \frac{d}{2} + \frac{2k-1}{2M} d\right)^2 \sin\varphi \begin{bmatrix} I_2 \\ I_3 \end{bmatrix} \qquad (5)$$

Besides, the attitude angular rate of carrier respect to inertial space is also the input angular rate of MSCSG, which is proportional to the coils current difference of LFMB [19].

$$\begin{cases} \omega_x = \dfrac{BL_r(I_4 - I_2)}{J_z \Omega} \\ \omega_y = \dfrac{BL_r(I_1 - I_3)}{J_z \Omega} \end{cases} \qquad (6)$$

Where, Ω is the rotation speed of rotor, J_z is the rotor's polar moment of inertia, ω_x and ω_y are the components of attitude angular rate (ω) at x-axis and y-axis. It is clearly that the precision of ω is directly decided by I and B.

The magnetic flux density at air gap of traditional LFMB is non-uniformly distributed. The flux density at the middle of axial gap is maximal and reduces along two sides of axial gap. The flux density at the rim of the axial gap is about half in the middle position. And the distribution of the flux density in radial direction is similar as well. So the magnetic flux density at air gap of basic LFMB is not uniform clearly [16]. Actually, the value of magnetic flux density (B_0) used for tilting control is just the magnetic flux density at the middle of the coils when it is at the balanced position. If the rotor tilts or translates, the coils deviate from the balanced position clearly. And the magnetic flux density at the middle of the coils must have changed, which is not equal to B_0. If the control current is still calculated by B_0, the rotor cannot be controlled accurately. And the precision of ω cannot be accurate as well.

$$P = \sum_{i=1}^{4} P_i = \sum_{i=1}^{4} I_i^2 R_i \qquad (7)$$

Where, P_i and R_i is the power consumption and resistance of coil i respectively. And R_i is a constant which has been determined after winding. Therefore, the only factor affecting the power consumption is the coil current. Combined with (5), in the case of generating the same magnetic torque, if B is smaller, coil current is larger and the power consumption is greater as well.

3.2. Design of basic LFMB and flux density analysis

Considering permanent magnetic flux leakage and magnetic circuit edge effect, the equivalent magnetic circuit for the basic LFMB is shown in Fig. 4. $F_{p1} \sim F_{p4}$ is the magneto motive force of the upper outside PM, the upper inside PM, the lower outside PM and the lower inside PM respectively. $F_{p1} \sim F_{p4}$ is the resistance of each PM respectively. R_{cu} and R_{cl} is the magnetic resistance of air gap through the coils for the upper and lower PMs. R_{gu} and R_{gl} is the magnetic resistance of air gap without through the coils for the upper and lower PMs. Φ_{cu} and Φ_{cl} is the total magnetic flux through the coils for the upper and lower air gap. Φ_{gu} and Φ_{gl} is the total magnetic flux without through the coils for the upper and lower air gap. The magnetic resistance of magnetic ring is ignored.

The total magnetic flux of the whole air gap is

$$\Phi=\begin{bmatrix}\Phi_{gu}\\ \Phi_{cu}\\ \Phi_{gl}\\ \Phi_{cl}\end{bmatrix}=\begin{bmatrix}R_{cu}/(R_{cu}+R_{gu})\\ R_{gu}/(R_{cu}+R_{gu})\\ R_{cl}/(R_{cl}+R_{gl})\\ R_{gl}/(R_{cl}+R_{gl})\end{bmatrix}\Phi_m \tag{8}$$

Where, Φ_m is the main magnetic flux for the air gap.

$$\Phi_m=\frac{\sum_{i=1}^{4}F_{pi}}{\sum_{i=1}^{4}R_{pi}+\frac{R_{cu}R_{gu}}{R_{cu}+R_{gu}}+\frac{R_{cl}R_{gl}}{R_{cl}+R_{gl}}} \tag{9}$$

The magneto motive force (F_{pi}) is

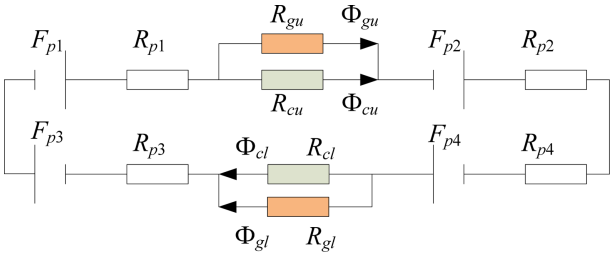

Fig. 4. (Color online) Equivalent magnetic circuit of basic LFMB.

$$F_{pi}=H_c l_{pi} \tag{10}$$

Where, H_c is coercive force of the PM and l_{pi} is the magnetization length.

The magnetic flux density calculated by magnetic flux for each position is

$$B=[B_{gu}\ B_{cu}\ B_{gl}\ B_{cl}]^T=diag(A_{gu}, A_{cu}, A_{gl}, A_{cl})^{-1}\Phi \tag{11}$$

Where, B_{cu} and B_{cl} is the magnetic flux density through the coils for the upper and lower air gap respectively, B_{gu} and B_{gl} is the magnetic flux density without through the coils for the upper and lower air gap respectively. A_{cu}, A_{cl}, A_{gu} and A_{gl} is the equivalent cross-sectional area for these 4 positions respectively.

Considering the symmetry of LFMB, there are $R_{cu}=R_{cl}=R_c$, $R_{gu}=R_{gl}=R_g$, $A_{cu}=A_{cl}=A_c$ and $A_{gu}=A_{gl}=A_g$. Then the magnetic flux density through the coils for the upper and lower air gap can be described as

$$B_u=B_l=\frac{2H_cR_gl_p}{2A_uR_p(R_g+R_c)+A_uR_gR_c} \tag{12}$$

As is known, samarium-cobalt (Sm2Co17) is one kind of rare earth PM with large BH product, reliable coercive force and high temperature resistance. Here, it is selected to be the PM of LFMB and its specifications can be seen in Table 1. Also, 1J50 is used for constructing the magnetic rings as a soft magnetic material and its characteristics are given in Table 2.

Based on the function and performance index of MSCSG, some main design parameters of LFMB I are shown in Table 3. As spaces limited, the specific design process is

Table 1. SM_2CO_{17} Characteristics.

B_r (T)	H_c (kA/m)	μ_r	$(BH)_{max}$ (KJ/m^3)	T_{max} (°C)	T_{ciure} (°C)
1.12-1.2	700-828	1.05	223-247	350	850

Table 2. 1J50 Characteristics.

B_s (T)	$\mu_{0.4}$ (mH/m)	μ_m (mH/m)	H_c (A/m)	ρ (μΩ·m)
1.5	≥ 5.0	≥ 65	≤ 8.8	0.45

Table 3. Main parameters of LFMB I.

Parameter (unit)	value	Parameter (unit)	value
inner diameter of the inside PM(mm)	103.4	axial length of coil (mm)	15
outer diameter of the inside PM (mm)	111.4	circumferential angle of a single coil (°)	84
inner diameter of the outside PM (mm)	124	number of turns for a single coil	210
outer diameter of the outside PM (mm)	132	coil space factor	49%
axial length of PM (mm)	11	resistance of a shingle coil (Ω)	14.3
axial distance between the upper and lower PM (mm)	4	amplitude of air gap flux density (T)	0.516

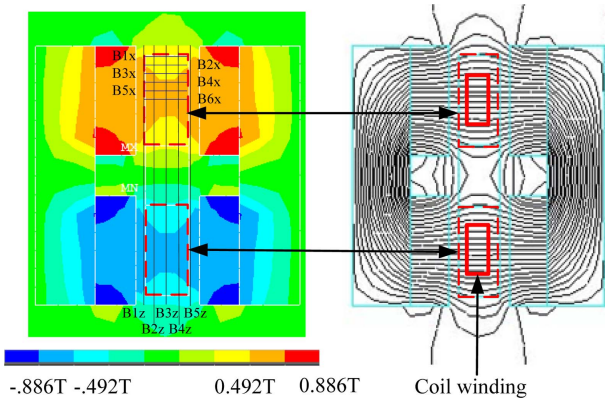

Fig. 5. (Color online) Graph of magnetic flux density cloud distribution and magnetic field line for LFMB I.

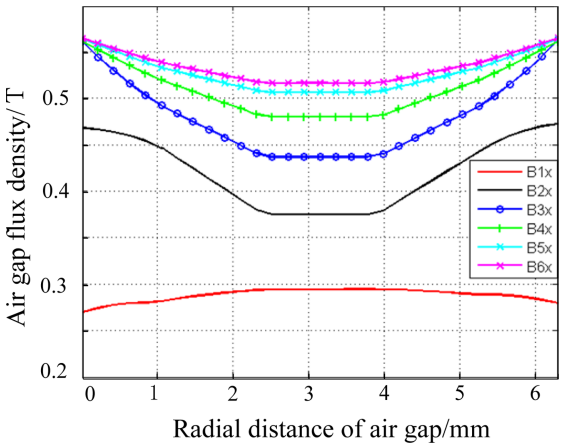

Fig. 6. (Color online) The magnetic flux density distribution in radial direction of the air gap for LFMB I.

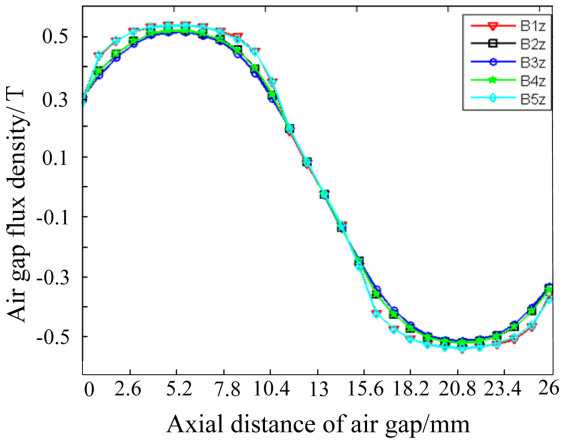

Fig. 7. (Color online) The distribution of magnetic flux density in axial direction of the air gap for LFMB I.

not described in detail.

The magnetic density cloud distribution and magnetic field line for LFMB I are shown in Fig. 5. The flux density at different positions in the air gap for the upper PMs in radial direction (B1x, B2x, B3x, B4x, B5x and B6x) is illustrated in Fig. 6 and these 6 radial positions are marked in Fig. 5. The distribution of magnetic flux density along the axial direction (B1z, B2z, B3z, B4z and B5z) can be seen in Fig. 7 and these 5 axial positions are also marked in Fig. 5. It is obvious that the air gap magnetic density is the largest in the middle of the air gap and decreases rapidly along both sides. In radial direction, the flux density at the middle of the air gap is smaller, and the two sides are larger. In axial direction, the flux density distribution in the whole air gap is similar to a sine curve. Obviously, the magnetic flux distribution is not uniform obviously.

4. Optimal Design of LFMB

4.1. Concept definition

It is clear that the precision of electromagnetic torque is directly determined by the distribution of air gap magnetic flux density of LFMB. And the power consumption of 4 coils is affected by the magnetic intensity. Here, the average value of flux density and the uniformity of air gap flux density are defined as follows.

The average value of flux density (B_{avg}) is defined as

$$B_{avg} = \frac{\sum_{i=1}^{N} B_i}{N} \tag{13}$$

Where, B_i is the flux density of one point at the working range, N is the number of the checked points. According to equation (5) and equation (7), the power consumption of LFMB can be smaller when the B_{avg} is larger.

The uniformity of air gap flux density (u_B) is employed to qualify the uniform degree of the air gap flux density distribution and the effective area is the working range of the coils when the rotor tilts or translates.

$$u_B = 1 - \frac{\delta_B}{B_{avg}} \tag{14}$$

Where, δ_B is the standard deviation of the flux density in the working range. And δ_B is described as

$$\delta_B = \sqrt{\frac{\sum_{i=1}^{N} (B_i - B_{avg})^2}{N-1}} \tag{15}$$

It is known that relative standard deviation (δ_B/B_{avg}) can be used to measure the dispersion degree of the data distribution based on mathematical expectation. u_B is

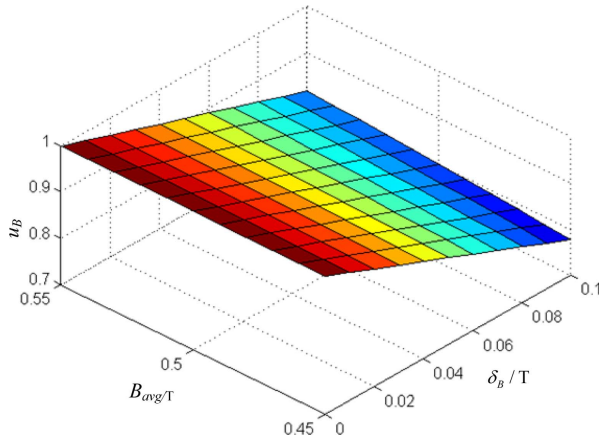

Fig. 8. (Color online) Relationship of u_B and B_{avg}, δ_B.

defined based on the relative standard deviation of air gap flux density in the working range, so the uniform degree of the air gap flux density distribution can be qualified. Obviously, the range of u_B is 0~1. The relationship between u_B and B_{avg}, δ_B is shown in Fig. 8. The larger the B_{avg}, the lower the power consumption of LFMB. The larger the u_B, the higher the precision of control and measurement. That is to say, the LFMB with high precision and low power consumption is better.

The magnetic flux density for coils is changing when the rotor tilts, as is shown in Fig. 9. δ is the tilting angle of rotor. According to the design index, the maximum tilting angle of MSCSG rotor is ± 1°.

Considering the relativity of motion, the tilting motion of rotor at balanced position can be regarded as the stator of LFMB tilting centered to the geometric center of gyro housing, as is shown in Fig. 10. O is the geometric center of gyro housing. P is the center of the upper part of one coil. When the rotor tilting without translation, the motion path is $\overset{\frown}{AB}$. Besides, the maximum displacement of the rotor translation is ± 0.2 mm. So the working range for the upper air gap is the covered area that $\overset{\frown}{AB}$ moves along the radial direction with ± 0.2 mm. The working range is the irregular quadrilateral *CDFE*. For the convenience of research, the working range can be expanded

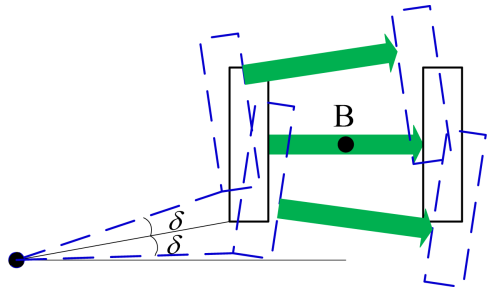

Fig. 9. (Color online) The moving area of rotor.

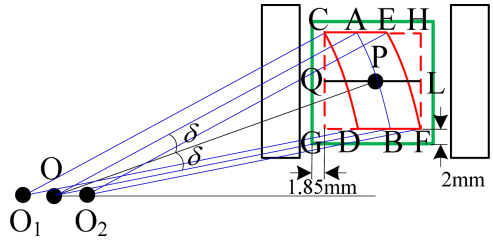

Fig. 10. (Color online) Equivalent graph of the motion of rotor.

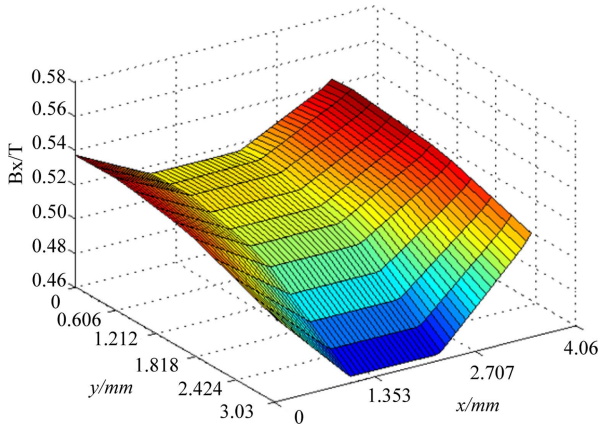

Fig. 11. (Color online) The distribution of magnetic flux density in the working range for the upper part of one coil for LFMB I.

to rectangle *CGFH*. Where, OP = 59.53 mm, CQ = 1.03 mm, QG = 1.04 mm, PQ = 0.34 mm, PL = 0.32 mm. Besides, the height and width of a section of one coil is 4 mm and 3.7 mm respectively. So the working range for the upper air gap can be expanded to the rectangle *C'G'F'H'*, which is the green rectangle in Fig. 10. And its height and width increased by 2 mm and 1.85 mm symmetrically based on *CGFH*. Obviously, this working range covers the whole area when the rotor tilts or translates.

It is clear that the distribution of magnetic flux density generated by upper and lower air gaps are axially symmetric without considering the direction of magnetic lines. Furthermore, the distribution for the upper (lower) air gap is also axially symmetric. Based on the axial symmetry, the uniformity of air gap flux density for the whole working range can be reflected by the upper half of rectangle *C'G'F'H'*. The distribution of magnetic flux density in the working range for the upper part of one coil for LFMB I can be shown in Fig. 11. It is clear that the distribution is not uniform. After calculation, u_B = 0.963 and B_{avg} = 0.503T.

4.2. Optimal design of LFMB

Based on some simulation analysis and experimental

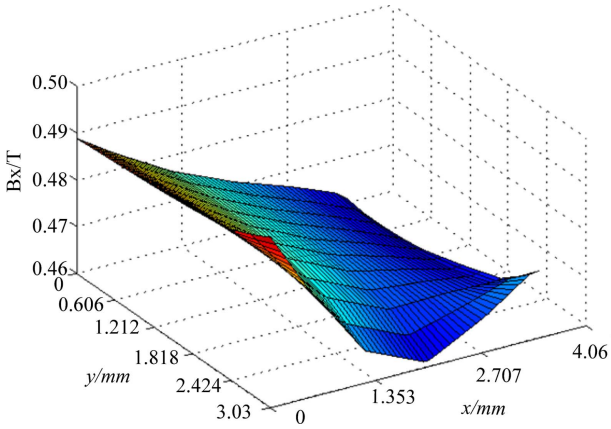

Fig. 12. (Color online) The distribution of magnetic flux density in the working range for the upper part of one coil for LFMB II.

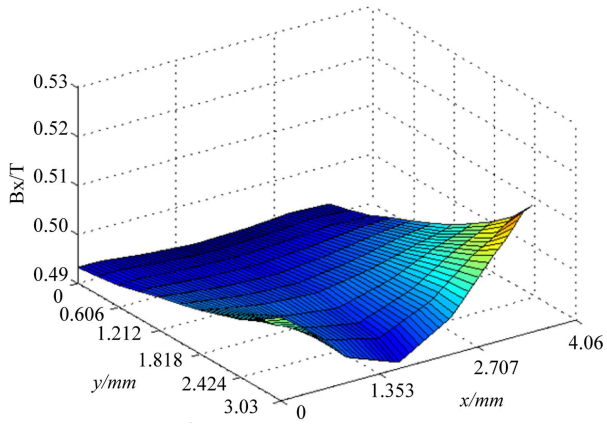

Fig. 14. (Color online) The distribution of magnetic flux density in the working range for the upper part of one coil for LFMB III.

studies, it is found that the uniformity of air gap flux density can be improved by attaching the 1J50 magnetic thin sheet to the surface of the PMs (LFMB II). As is known, 1J50 is one kind of Fe-Ni soft magnetic alloy with high magnetic permeability and small coercive force under weak magnetic field. Attaching 1J50 thin magnetic sheet to the surface of the PM can make the air gap become smaller. Due to its high permeability, the magnetic lines are perpendicular to its surface. So the distribution of the magnetic lines can become more uniform. The distribution of magnetic flux density at the working range for LFMB II is shown in Fig. 12.

Compared with LFMB I, the distribution of LFMB II is much more uniform obviously. As is known, the total magnetic flux remains unchanged. The distribution of the magnetic flux density is not uniform and the magnetic flux density of working range of the coils for LFMB I is higher than other area at the air gap. So the B_{avg} of LFMB II is smaller than LFMB I at the working range. After calculation, $u_B = 0.983$ and $B_{avg} = 0.473$T.

As mentioned before, the power consumption of LFMB can be higher if the B_{avg} is smaller. So some further optimal designs should be carried out to improve the B_{avg}. Obviously, the magnetic density can become stronger if the magnetic area is lager. Based on this, a new shape of PM is put forward and a new LFMB (LFMB III) is designed, as is shown in Fig. 13.

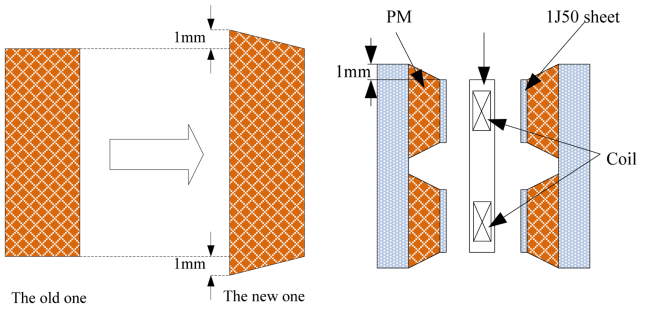

(a) The change of the shape for PM (b) Section schematic of LFMB Ⅲ

Fig. 13. (Color online) Configuration of LFMB III.

Compared to LFMB II, the magnetic area of LFMB III becomes larger and the total magnetic flux becomes larger as well. So the B_{avg} of LFMB III can get improved obviously. And modifying the PM shape affects the uniformity of flux density little. The distribution of magnetic flux density at the working range for LFMB III is shown in Fig. 14. After calculation, $u_B = 0.992$ and $B_{avg} = 0.498$T. Here, u_B (LFMB III) > u_B (LFMB II) and B_{avg} (LFMB III) > B_{avg} (LFMB II), so LFMB III is better and can be selected temporarily. The designed rotational speed of the MSCSG rotor is 10 000 r/min. So the trapezoidal PMs are easier to limit and maintain stable when the rotor rotates in high speed, especially the inside PMs.

The trapezoidal PM rings are composed of pieces of PMs and fixed to the rotor by the middle integral magnetic separation ring and lock nut on the upper and lower ends. So the inside PM ring can avoid radial motion caused by centrifugal force generated by high speed rotation of rotor.

4.3. The strength of the PM affects the machining

The PM is made by casting or sintering and its structure of the molecule is grain. The hardness and brittleness of the magnet is high, which is easy to crack under high frequency impact. So the diamond grinding wheel with high hardness is usually adopted to machine. Both the friction and relative extrusion are between the wheel and the magnetic steel. Because the spindle of the wheel has a

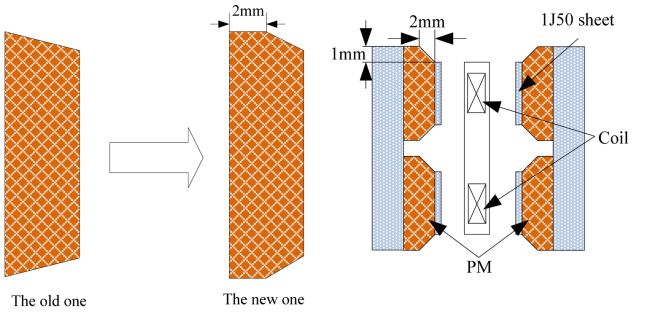

(a) The change of the shape for PM (b) Section schematic of LFMB Ⅳ

Fig. 15. (Color online) Configuration of LFMB IV.

micro beating while the wheel is rotating, not only there will be relative friction between the grinding wheel and the magnet during the grinding process but also some impact at the same. The rotation speed of the spindle is high and the frequency of impact caused by the beating of the spindle is high as well which will bring some fragmentation to the PM. The strength of the both ends of PM for LFMB III is relatively low and is easy to crack when it is impacted with same frequency. It is clear that the design of LFMB III has some disadvantages. To avoid the fragmentation of PM, something should be done to increase the local thickness and enhance the strength at the both ends of the PM without increasing the thickness of the overall design. Based on this, a new design (LFMB IV) is shown in Fig. 15.

Compared to LFMB III, the PMs of LFMB IV are relatively thicker at both ends and the total magnetic flux becomes larger surely. The distribution of magnetic flux density at the working range for LFMB IV is shown in Fig. 16. After calculation, u_B = 0.995, and B_{avg} = 0.506T. All the indexes of LFMB IV are better than all previous designs, so LFMB IV is selected to be the final one.

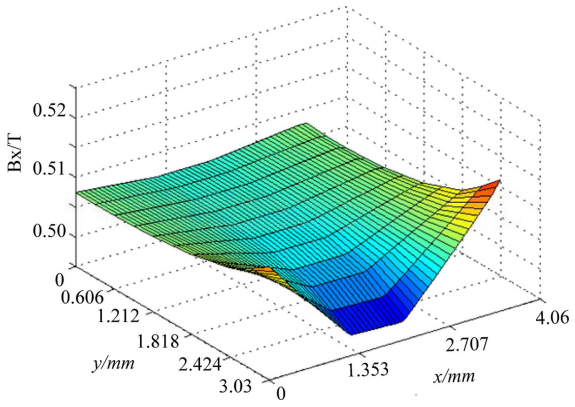

Fig. 16. (Color online) The distribution of magnetic flux density in the working range for the upper part of one coil for LFMB IV.

Table 4. Key performances of 4 LFMBs.

	LFMB I	LFMB II	LFMB III	LFMB IV
B_{avg}(T)	0.503	0.473	0.498	0.506
u_B	0.963	0.983	0.992	0.995
stability	poor	poor	good	good

Some key performances of these 4 LFMBs are summarized in Table 4. It is obvious that LFMB IV is the best one. The stability means that the PMs are easier to limit and maintain stable when the rotor rotates in high speed.

5. Measurement of the Magnetic Flux Density for LFMB

Based on the design of LFMB IV, LFMB has been machined with magnetized magnets. To validate the design and machining effect, a high-precision instrument is employed to measure the 3-dimensional magnetic flux

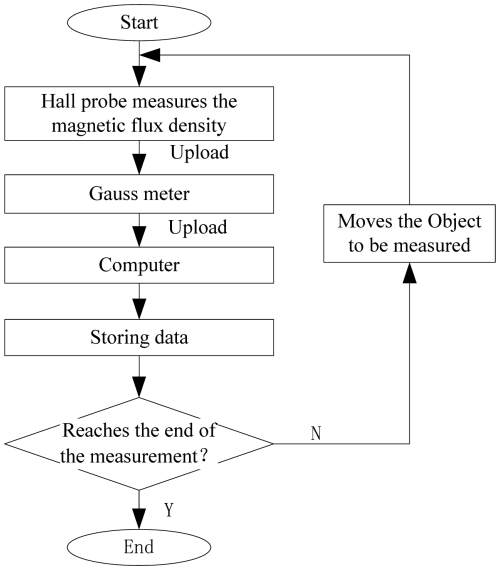

Fig. 17. The workflow of the measuring instrument for magnetic flux density.

Table 5. Main parameters of measurement scheme.

Parameter (unit)	value	Parameter (unit)	value
diameter of hall probe (mm)	2	single-step circumferential displacement (°)	2
measuring accuracy of hall probe (mT)	0.01	single-step radial displacement (mm)	1
positioning accuracy of hall probe (mm)	0.0039	single-step axial displacement (mm)	1

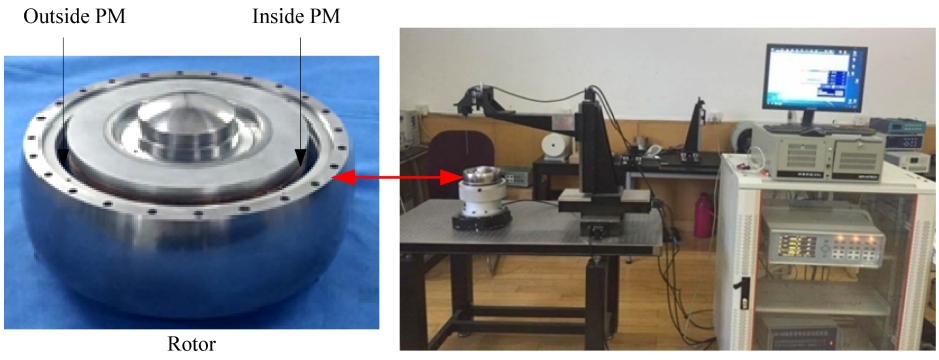

Fig. 18. (Color online) The measurement of the magnetic flux density for LFMB.

density of the machined LFMB. The measuring instrument consists of computer (with control software), high-precision gauss meter, 3-dimensional hall probe, electronic controlled multidimensional displacement station as well as its controller. Its workflow is shown in Figure 17.

The main parameters of measurement scheme for LFMB are shown in Table 5. The actual measurement is divided into 4 steps: (1) The radial position is selected; (2) The magnetic flux density is measured along the circumferential direction and the single-step displacement is 2°; (3) The hall probe moves down along the axial direction and the single-step displacement is 1 mm; (4) Repeat step (2) until the hall probe reaches the ends.

The measurement of the magnetic flux density for LFMB is carried out and shown in Fig. 18.

According to the measurement scheme, the hall probe moved in circles with different radius in the air gap. Limited to the size of the hall probe, the radius can only be set to 59.85 mm, 58.85 mm and 57.85 mm. The measured results of the upper and lower parts of the working range for coils are shown in Fig. 19 and Fig. 20 respectively. Where, $x = radius \times \sin\theta$, $y = radius \times \sin\theta$ and $\theta \in [0; 2\pi]$.

Based on these results, the average value of the flux

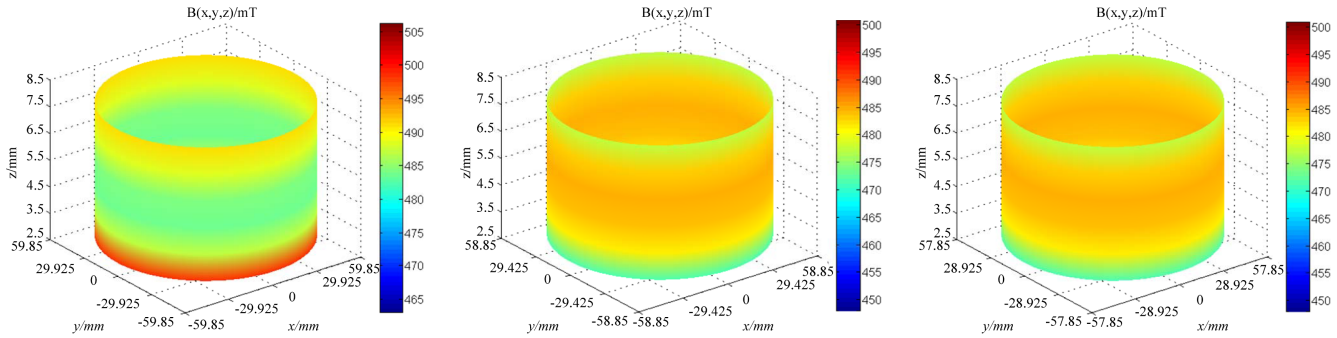

(a) radius=59.85mm (b) radius=58.85mm (c) radius=57.85mm

Fig. 19. (Color online) The measured results for the upper part of the working range.

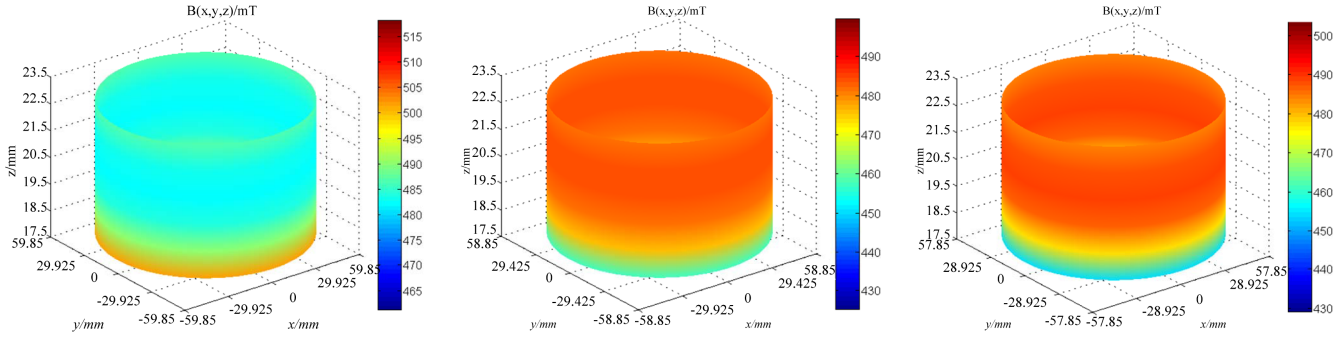

(a) radius=59.85mm (b) radius=58.85mm (c) radius=57.85mm

Fig. 20. (Color online) The measured results for the lower part of the working range.

Table 6. Calculated results based on measured results.

	Upper part			average	Lower part			average	Entire working range	
	59.85 mm	58.85 mm	57.85 mm		59.85 mm	58.85 mm	57.85 mm		calculated value	desired value
B_{avg} (T)	0.485	0.479	0.482	0.482	0.487	0.478	0.482	0.482	0.482	0.506
u_B	0.984	0.981	0.978	0.981	0.981	0.972	0.971	0.975	0.978	0.995

density (B_{avg}) and the uniformity of air gap flux density (u_B) for each measured result can be calculated in Table 6.

The u_B of the entire working range is 0.978, which is larger than the basic LFMB (0.963). It is clear that the validity of the optimal design is proved. But the u_B is 1.7 percent smaller the desired value (0.995) of LFMB IV. This is because each PM ring is spliced with 12 small pieces, which are magnetized respectively. Obviously, the consistency of magnetizing effect cannot be guaranteed. So the uniformity of air gap magnetic flux density is reduced to some extent.

At the same time, the average value of the flux density (0.482T) is 4.7 percent smaller than the desired value (0.506T) of LFMB IV. Based on the designed magnetizing intensity, the magnetic density cannot achieve the design goal. So, to meet the goal, the value of magnetizing intensity should be enlarged properly.

6. Conclusion

To design a new LFMB with high-precision and low power consumption, the magnetic flux density distribution and magnetic intensity for LFMB is studied. The uniformity of air gap flux density is defined to quantify the uniform degree of the magnetic flux density distribution and the average value of magnetic flux density is used to select the LFMB with larger magnetic density. It is found that the uniformity of air gap flux density can be improved by attaching the 1J50 magnetic thin sheet to the surface of the PMs and the distribution intensity of magnetic density is affected by changing the shape of the PMs. Some optimal designs are carried out by finite element simulation analysis. And the strength of the PM is taken in to account during the specific machining process. After measurement and calculation, the uniform degree of magnetic flux density distribution reaches 0.978 and the average value of the flux density is 0.482T. Experimental results show that the optimal design is effective and some useful advice can be obtained for further research.

Acknowledgements

This work was supported by the National Natural Science Foundation of China under grant of 51475472 and 61403396.

References

[1] J. Tang, B. Liu, J. Fang, and S. S. Ge, J. Vib. Control. **19**, 1962 (2013).
[2] G. Liu, J. Fang, and J. Liu, Aerospace Control **41**, 88 (2008).
[3] X. Chen and Y. Ren, Proc IMechE Part C :J. Mechanical Engineering Science **228**, 2303 (2014).
[4] J. C. Ji, C. H. Hansen, and A. C. Zander, J. Intell. Mater. Syst. Struct. **19**, 1471 (2008).
[5] T. Wei, J. Fang, and Z. Liu, Journal of Mechanical Engineering **46**, 159 (2010).
[6] J. Fang, S. Zheng, and B. Han, IEEE/ASME Trans. Mechatron. **18**, 32 (2013).
[7] Y. Ren and J. Fang, IEEE Trans. Ind. Electron. **59**, 4590 (2012).
[8] Y. Ren and J. Fang, IEEE Trans. Ind. Electron. **61**, 1539 (2014).
[9] J. Fang, J. Sun, and Y. Fan, Magnetically Suspended Inertial Momentum Wheel Technology, National Defense Industry Press, Beijing (2012) pp. 9-10.
[10] Y. Maruyama, M. Takasaki, Y. Ishino, M. Takasaki, T. Ishigami, and H. Kameno, Japan Joint Automatic Control Conference (2006).
[11] Y. Maruyama, T. Mizuno, M. Takasaki, Y. Ishino, T. Ishigami, and H. Kameno, Journal of System Design and Dynamics **2**, 155 (2008).
[12] S. H. Park and C. W Lee, IEEE/ASME Trans. Mechatron. **10**, 618 (2004).
[13] L. S. Stephens and D. G. Kim, IEEE Trans. Magn. **38**, 1764 (2002).
[14] H. Y. Kim, C. W. Lee, Mechatronics **16**, 13 (2006).
[15] N. Kurita, T. Ishikawa, and M. Matsunami, 2009 International Conference on Electrical Machines and Systems, 1 (2009).
[16] Y. J. Yu, J. C. Fang, B. Xiang, and C. E. Wang, ISA Trans. **53**, 1892 (2014).
[17] J. Abrahamsson, J. Ogren, and M. Hedlund, IEEE Trans. Magn. **50**, 1 (2013).
[18] B. Xiang and J. Tang, Mechatronics **28**, 46 (2015).
[19] B. Liu and J. Fang, Hangkong Xuebao/acta Aeronautica Et Astronautica Sinica **32**, 1478 (2011).